Post-Print

This is the accepted version of:

The final publication is available at https://doi.org/10.1109/TGRS.2023.3268560

Access to the published version may require subscription.

When citing this work, cite the original published paper.

Permanent link to this version
http://hdl.handle.net/11311/1236504

TriHex: combining formation flying, general circular orbits and alias-free imaging, for high resolution L-band aperture synthesis

Manuel Martin-Neira, *Senior, IEEE*, Francesca Scala, Albert Zurita, Martin Suess, Miguel Piera, Berthyl Duesmann, Matthias Drusch, Camilla Colombo, Don de Wilde, Josep Closa, Erio Gandini, *Senior, IEEE*, Raúl Díez-García, *Graduate Student Member, IEEE*, Roger Oliva, *Member, IEEE*, and Ignasi Corbella

Abstract—**ESA's Soil Moisture and Ocean Salinity (SMOS) mission, together with NASA's Soil Moisture Active Passive (SMAP) mission, are both providing a wealth of information to the user community for a wide range of applications. Although both missions are still operational, they have significantly exceeded their design life time. For this reason, ESA is looking at future mission concepts which would adequately address the requirements of the passive L-band community beyond SMOS and SMAP. This paper proposes one mission concept, TriHex, that has been found capable of achieving high spatial resolution, radiometric resolution and accuracy, approaching the user needs. This is possible by the combination of aperture synthesis, formation flying, the use of general circular orbits and alias free imaging.**

Index Terms—**Aperture Synthesis, Formation Flying, General Circular Orbits, SMOS**

I. INTRODUCTION

SOON after the SMOS (Soil Moisture and Ocean Salinity) project started at the European Space Agency in the early 2000's [1][2], consideration was already given to a follow-on mission. To guarantee users with L-band observations for a period longer than 10 years and noting that the design life of SMOS was 3 years, the SMOSops mission was proposed in 2004 consisting of 3 identical copies of SMOS (Fig. 1) [3]. However, SMOSops was never approved and SMOS was launched on November 2nd, 2009.

The very first images provided by SMOS showed very apparently the problem of radio frequency interference (RFI) (Fig.2). Not only the pixels at the location of the RFIs were corrupted, but also many others affected by the sidelobes of the impulse response of the Microwave Imaging Radiometer with Aperture Synthesis (MIRAS), the payload on board SMOS. A study on a Super-MIRAS instrument showed the tight relationship between the array geometry and the amplitude of the sidelobes [4]. In particular, closed figures as polygons lead to lower tails of secondary lobes than open geometries, like the Y-shape of SMOS. For this reason, a hexagon was proposed in 2012 (Fig. 1) as a much better shape for any SMOS follow-on mission, to focus the RFI energy avoiding the spill over across the image through long tails of secondary lobes. Furthermore, because of the greater extent provided by the hexagon in the visibility domain by comparison to the Y-shape (of the same arm length), a 18.3% spatial resolution improvement was expected (at the cost of doubling the number of receivers). A hexagonal instrument of a similar size to that of SMOS (7.8 m diameter), dubbed SMOSops Hexagonal, was studied in detail in [5].

SMOSops Hexagonal presented two additional differences with respect to SMOS. First, a smaller spacing between antenna elements of 0.767λ (0.875λ in SMOS), which allowed enlarging the alias-free swath to 946 km (587 km in SMOS). Second, a reduced pitch angle of 21° (32.5° in SMOS) because, with the wider alias-free swath, there was no need to go for larger pitch angles to ensure good incidence angle coverage. With all its features, the estimated spatial resolution SMOSops would attain at boresight came to 33 km (41 km for SMOS).

Despite the improvements, SMOSops Hexagonal mission concept fell short in addressing one key user requirement for a future L-band observation system, namely an improved native spatial resolution approaching the 10 km × 10 km goal [6].

This paper presents the steps that have been taken following an extensive user consultation including a requirement consolidation [6], [7] to evolve from the SMOSops Hexagonal to a new mission concept approaching the desired spatial resolution.

To complete this introduction, a couple of comments. One is

M. Martín-Neira is with ESA, Noordwijk, The Netherlands (manuel.martin-neira@esa.int).

F. Scala and C. Colombo are with Politécnico di Milano, Italy.

A. Zurita, M. Piera and J. Closa are with Airbus Defense and Space, Madrid, Spain.

M. Suess, B. Duesmann, M. Drusch, Don de Wilde and Erio Gandini are with ESA, Noordwijk, The Netherlands.

R. Díez-García is with Telespazio UK Ltd, ESAC, Villanueva de la Cañada, Spain.

R. Oliva is with Zenithal Blue Technologies, Barcelona, Spain.

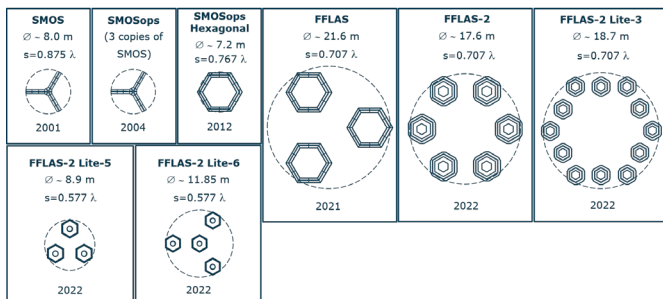I. Corbella is with Polytechnic University of Catalunya, Barcelona, Spain.

Fig. 1. Upper row, from left to right: SMOS, started in 2001; SMOSops, proposed in 2004, consisting of 3 identical copies of SMOS; SMOSops Hexagonal studied in 2012 would better focus RFI sources; Formation Flying L-band Aperture Synthesis (FFLAS) is introduced in 2021 to reach 10 km ground resolution; FFLAS-2 is a variation of FFLAS, studied in 2022 as the rest of the configurations, that avoids the deployment of the hexagons by using smaller spacecraft that fit in the fairing of an Ariane 6 rocket; FFLAS-2 Lite-3 is yet a further variation which can be launched with the less costly VEGA launcher, leveraging the break-up of the formation into smaller hexagons; Lower row: FFLAS-2 Lite-5 and Lite-6 are cost-effective formations that use alias-free spacing, the former being the focus of this paper.
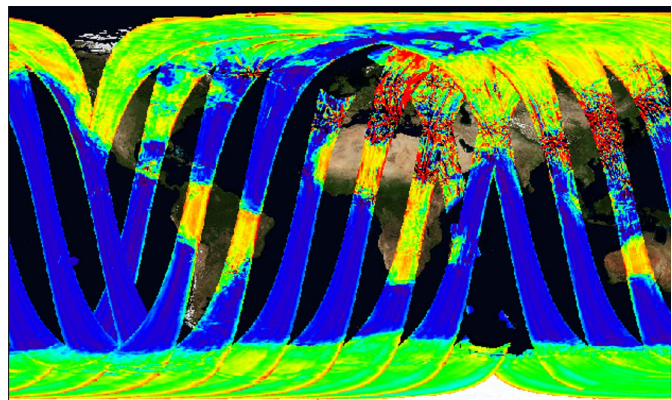

Fig. 2. First browse product swath-based image produced by SMOS, on 19-Nov-2009, showing the brightness temperature at a fixed incidence angle of 42.5°. The red pixels represent anomalous high values of brightness temperature as a consequence of Radio Frequency Interference (RFI). It was observed that not only the pixel where the RFI is located is polluted, but also many other pixels around it due to the sidelobes of the impulse response of Y-shaped MIRAS, the instrument on board SMOS. The reason to propose an hexagon in SMOSops Hexagonal was to significantly reduce the sidelobes and hence, the spread of RFI energy to other pixels in the image.

on the status of the L-band radiometers. By the time of the writing of this paper, SMOS is still operational, after 13 years in orbit, and NASA's SMAP (Soil Moisture Active Passive) mission, launched on January 31st, 2015, is also fully working, after almost 8 years in space [8]. The second comment is about the user requirements. These have been more recently reviewed by the Global Climate Observing System [9]: 10 km is the goal and break-through spatial resolution requirements for Sea Surface Salinity and Soil Moisture respectively, with 1 km being the goal for the latter.

II. Enlarging the Aperture by Formation Flying

From the 33 km boresight spatial resolution of the 7.8 m diameter SMOSops Hexagonal one can conclude, by simple linear scaling, and with all other system parameters unchanged, that an aperture of about 25 m is needed to meet the 10 km resolution recommended at the ECMWF workshop. Given the enormous challenge of accommodating, launching, and deploying such a large hexagonal array in space, a different approach to a large single aperture was considered, that of a formation of smaller instruments.

In 2021 a study on Formation Flying L-band Aperture Synthesis (FFLAS) was carried out in ESA. It was found that an arrangement of three hexagons properly oriented at the vertices of an equilateral triangle led to good coverage in the visibility domain and to an impulse response with low sidelobes. Therefore, one such formation consisting of three spacecraft identical to SMOSops Hexagonal was studied in detail (Fig. 1).

Although FFLAS could obtain the required 10 km ground resolution, it was at the expense of four costly elements and the challenge brough by unconnected interferometry. First, each hexagon had to be deployable to fit inside the launcher fairing, as in [5], increasing design complexity and mass significantly. Second, in order to maintain a rigid formation, forced motion was proposed, leading to a large mass of propellant being

required over a 10-year lifetime. The amount of fuel, together with the tanks, thrusters, and pipes, had a high mass impact. Third, for better brightness temperature accuracy, two rows of dummy elements were assumed implementing the antenna pattern equalization approach in [10], also adding to the mass budget. Finally, because of the large total mass (over 1,600 kg per hexagon) and volume of the spacecraft, an Ariane 6 launcher had to be chosen, more expensive than other smaller launchers.

To reduce cost, two variants of FFLAS were considered from a very preliminary system level perspective: FFLAS-2 and FFLAS-2 Lite-3 (Fig. 1). FFLAS-2 removed the need for deployable hexagons by splitting the formation into six smaller hexagons, each fitting in a single piece inside the fairing of Ariane 6. FFLAS-2 Lite-3, in addition, removed the need for a big launcher by further increasing the number of hexagons to twelve, while reducing the size of each of them. These smaller hexagons would fit within the more cost-effective VEGA launcher, although two launches would be required to bring the full formation in orbit.

Still the rough order of magnitude cost of FFLAS-2 and FFLAS-2 Lite-3 was deemed to be too high, and the efforts focused on coming up with a more cost-effective formation while pursuing the scientific objectives. The path that was followed and the final results are described in the next sections.

III. The General Circular Orbits: a Breakthrough

During the FFLAS study a careful look at the orbital dynamics of the formation was taken. After the FFLAS study was completed, the analysis of the orbits was yet continued within ESA. The outcome of this follow-on research was a breakthrough for the application of formation flying L-band aperture synthesis: the General Circular Orbits (GCO).

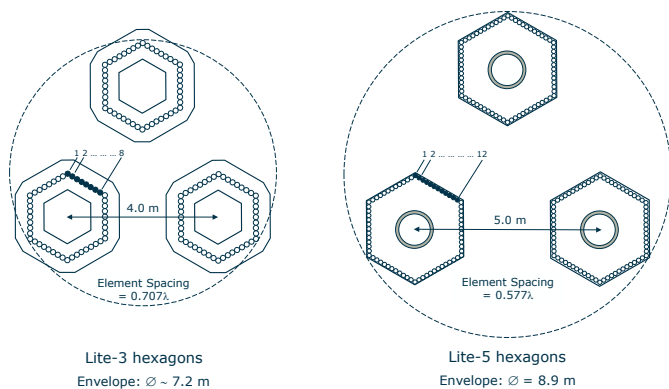The GCO are described in detail in [11] and [12]. In

Fig. 3. This figure shows the increase in aperture size achieved in the Lite-5 configuration (right) by placing the antenna elements at the rim of the hexagons instead of in the center line of the ground plane as in the Lite-3 hexagons (left). The reduction of element spacing from 0.707λ in Lite-3 to the alias-free spacing of 0.577λ in Lite-5 makes the image processing robust against residual antenna pattern differences.
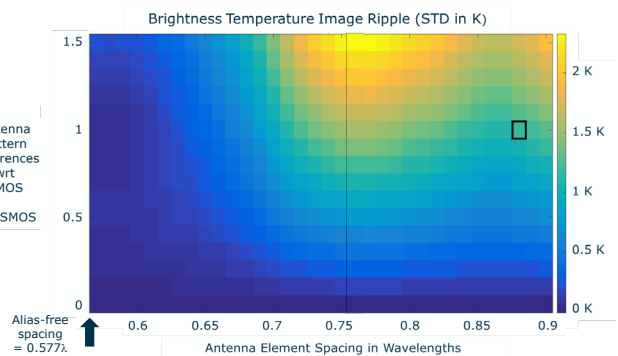

Fig. 4. Simulated standard deviation (STD) of the spatial ripple (in the alias-free field of view) of the brightness temperature image of the ocean of an SMOS-like instrument. The ripple STD is plotted as a function of the antenna element spacing and the antenna pattern dispersion (measured normalized to that of the patterns of the SMOS elements). This simulation results are consistent with Fig.4 in [41]. The square indicates the SMOS case.

summary, applying small variations on the Keplerian parameters of the orbit of a virtual reference point at the center of the formation, one can find a set of orbits for the spacecraft of the formation (the number of spacecrafts is unlimited). Then, by applying certain conditions, such set of orbits guarantees that the centers of mass of all the spacecraft lie on the same plane and rotate, once per orbit, around the reference point of the formation. The plane of the centers of mass is rolled by about 30° when the reference point follows the same orbit as SMOS, i.e. a 775 km mean altitude Sun synchronous orbit, with a Local Time of Ascending Node of 6:00 AM. Of the two possible 30° roll angle solutions, clock- and counter-clockwise, the latter solution is chosen. Then the Sun shines on the back side of the rolled spacecraft, their front sides pointing towards the dark side defined by the terminator, a desired geometry from the radiometric point of view.

The fundamental feature of the GCOs is that these are natural orbits, and the formation is ideally self-maintained through gravity, without the need of any thrust. Obviously, some thrust is still required to counter differential external forces applied on the spacecraft from the Earth's aspherical gravitational potential, Sun radiation pressure, and atmospheric drag, mainly. The net result is that the amount of fuel drops dramatically when compared to that which was needed in the original forced FFLAS formation. The amount of fuel has been estimated to be a factor 20 smaller [12]. Still some additional fuel is required for orbit keeping of the reference point, formation acquisition, Cold Sky calibration manoeuvres, debris avoidance, safe mode and end of life disposal. In any case, thanks to the GCOs, the net reduction in fuel mass and propulsion system elements is expected to be very pronounced.

For the TriHex concept, a continuous control approach has been implemented. This allows a continuous compensation of relative orbit variations due to the external perturbations of its Low Earth Orbit. In this way, the relative distance is continuously controlled and maintained in its correct range, removing the uncertainties due to the impulsive manoeuvres. This is the most important difference in terms of safety and

maintenance considerations between TriHex and prior formation concepts as those in [13] and [14].

Another major advantage of using natural orbits is the much longer time the operations team can have to react in case of failure of one or more of the satellites of the formation. In the forced motion case of the original FFLAS formation, if one spacecraft fails, the reaction time is very much limited, of the order of half the orbital period (i.e. about 50 minutes). For this reason, an on-board mechanism was proposed in FFLAS to bring the active spacecraft into safe mode autonomously. When using GCOs the constellation continues in formation for a considerably more extended period, in the scale of days. Therefore, autonomous safe mode can also be implemented on-board but with far more ample margins, resulting in a less critical situation from the operations point of view. Given the importance of safety strategies, future development of the TriHex concept will focus on the design of both autonomous and ground-based techniques.

For what concerns the roll of the plane of the centers of mass of the spacecraft, a similar configuration, in terms of applying a roll angle to the spacecraft to have the Sun at the back, was in fact studied for the SMOSops Hexagonal in [5]. The interest of such configuration will become clear later in the paper. The conclusion of that study was that, when rolling the spacecraft, a substantial reduction in the number of pixels within the alias-free field of view was experienced, making such configuration unpractical.

However, recognizing that the loss of pixels of the rolled SMOSops Hexagonal was due to the limited extent of the alias-free field of view, one can deduce that, in the absence of aliases, a rolled or a pitched spacecraft would view the same number of pixels. Therefore, the attention turned onto the antenna element spacing, as this parameter determines whether or not there is, as well as the size of, the alias regions in the field of view of the interferometer. This is explained in the next section.

IV. ALIAS-FREE IMAGING

In two-dimensional interferometry with visibility samples at the points of a regular hexagonal grid, the alias-free condition
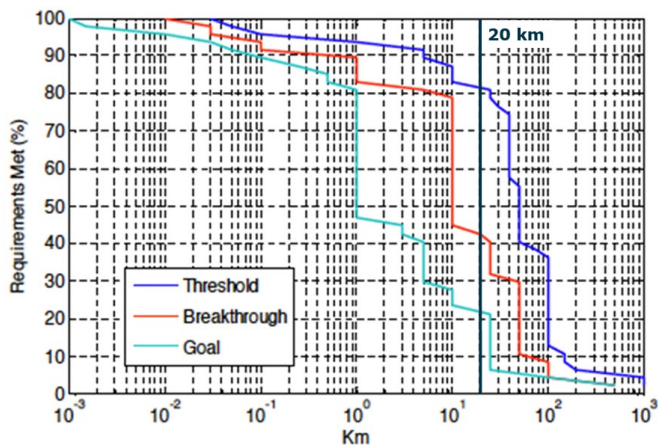
Fig. 5. Percentage of user requirements fulfilled as a function of the spatial resolution of passive L-band observations, from the set of applications collected in [7]. About 80% of user requirements are satisfied with 20 km resolution measurements. (Note: Requirements are provided with three values: threshold, breakthrough and goal. If a requirement at the threshold value cannot be met then the corresponding science data are of little to no value, meaning that the system is not fit for its intended purpose. If a requirement can be met at the breakthrough level, the intended applications can be fully addressed. The goal requirement characterises a performance that allows to advance science and applications beyond expectations.)

is just met when the normalized spacing between them, s, equals [15]

$$s = \frac{1}{\sqrt{3}} = 0.57735... \quad (1)$$

To achieve such sampling spacing it is necessary that the antenna elements, arranged along the hexagonal arrays in the configurations of Fig. 1, be separated by $s\lambda$ (in SMOS, a longer spacing s=0.875 was used, as a trade-off among swath, defined as the region free from Earth aliases, number of receivers and antenna coupling). If this is fulfilled, then the rolled formation produced naturally by the GCO of the previous section would not suffer of any loss of pixels in the field of view by comparison to a pitched configuration as the one of SMOS.

It is then seen how well the alias-free imaging fits together with the GCOs in that the natural orbits can now be used in a practical situation without any loss of coverage (because of the roll angle), provided the element spacing respects (1).

As soon as it was established that the advantageous GCOs became very practical when combined with the alias-free imaging, two new satellite formations were proposed, the FFLAS-2 Lite-5 and the FFLAS-2 Lite-6 in Fig. 1, with their elements spaced according to (1). Both these configurations follow the same approach as that of FFLAS-2 Lite-3 in that the hexagonal spacecraft fit the fairing of a small launcher like VEGA, not requiring any deployment. Out of these two formations, to minimize cost, the FFLAS-2 Lite-5 was then chosen for further assessment.

The problem with the FFLAS-2 Lite-3 hexagons, when directly used to make a formation of three hexagons, is the relatively small final aperture (7.2 m), as shown on the left of Fig. 3. However, here again, the implementation of the alias-

free spacing comes to one's advantage in that the antenna elements can be placed at the rim of the hexagons, instead of at the center of the ground plane, without performance degradation. The explanation is given in the next paragraphs. The new final aperture FFLAS-2 Lite-5 can achieve, illustrated on the right of Fig. 3, becomes quite larger (8.9 m).

The advantages of alias-free imaging became clear while studying the reason behind the spatial ripples existing in the SMOS images, of about 1 K (standard deviation) amplitude. In that study [16], complete simulations were carried out to assess the standard deviation of the ripple (in the alias-free field of view) of an image of the ocean taken by a noiseless SMOS-like instrument. The magnitude of the ripple was analyzed as a function of antenna element spacing and antenna pattern similarity. Pattern differences of variable amplitude were introduced artificially, normalized to the SMOS case. A representative result of the study is given in Fig. 4. As shown, when the antenna element spacing is set to the alias-free spacing, the amplitude of the spatial ripple in the image is very low regardless of the dispersion between antenna patterns. This means that, although the antenna patterns of the elements next to the rim (as in FFLAS-2 Lite-5) are expected to be less similar to those of the elements in the center line of the ground plane (as in FFLAS-2 Lite-3), the absence of aliases in the first case guarantees little impact in the images produced.

Noise propagation was not studied in [16]. A recent publication discusses in detail this matter, pointing to the fact that alias-free conditions may induce worse noise propagation than aliased imaging due to an increase of the condition number of the reconstruction matrix [17]. A full analysis of image reconstruction for Tri-Hex is still to be done, but a preliminary analysis using Y-shaped geometries (and discarding redundant baselines) indicate that, although the condition number for alias-free is worse than in aliased conditions, the problem is well-posed and stable.

It is important to mention here that ESA is conducting the predevelopment of a small antenna with a diameter of 0.577λ that allows alias-free imaging. This antenna, for which the design and preliminary simulations are ready, enables the alias-free imaging condition. Further confirmation of the imaging performance when the antennas are placed at the rim of the hexagon are also expected to be carried out by using real pattern measurements into an instrument simulator and ground processor.

V. THE TRIHEX MISSION CONCEPT

Following the success of the SMOS mission, ESA initiated a requirement consolidation activity based on careful review of demonstrated applications and envisaged future developments until 2025 [7a]. Almost 50 individual applications were analyzed and assessed together with the respective communities with a focus on measurement uncertainty, spatial resolution, and temporal revisit time. Finally, a cluster analysis was performed for a quantitative assessment of future requirements [7b]. The threshold requirements for spatial resolution, temporal resolution, and radiometric accuracy were 25 km × 25
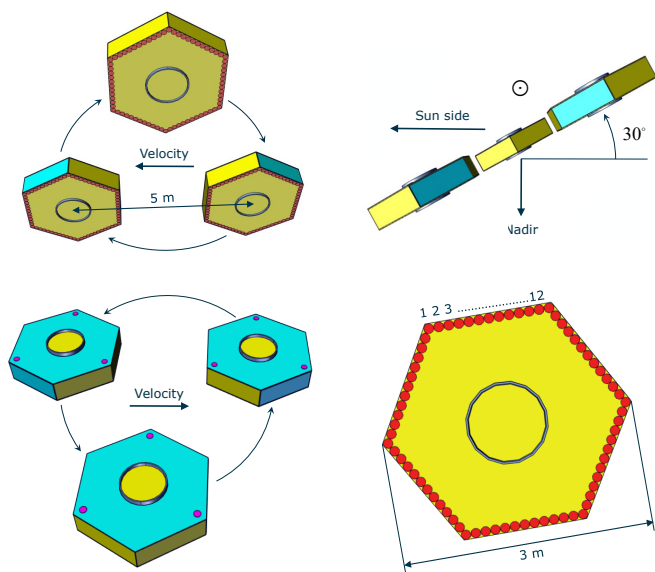
Fig. 6. TriHex formation viewed from the Earth (left top), from the Sun (left bottom), and from the velocity direction (right top). Front face of the spacecraft with the array of antennas at the rim (right bottom).
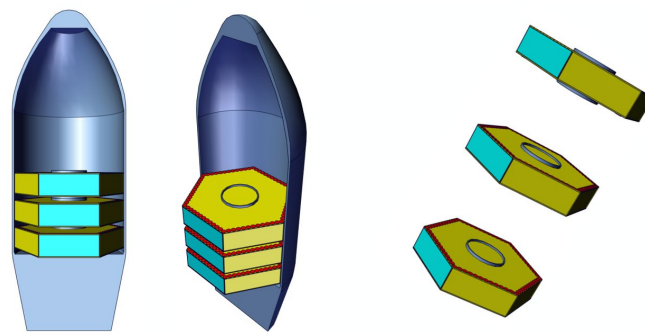

Fig. 7. TriHex satellites accommodated inside the fairing of a VEGA launcher (left), and view of those, shortly after they are released (right).
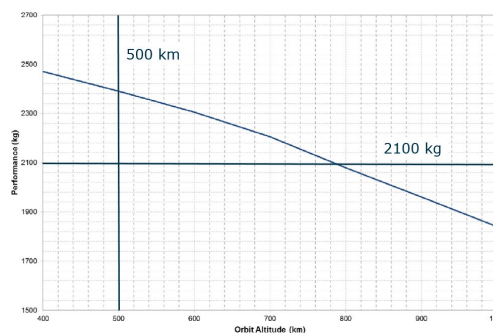

Fig. 8. Vega C launch vehicle performance data (including adapter) for sun-synchronous orbit (SSO) missions as a function of altitude (taken from [19]). A total mass of 2400 kg is allowed at 500 km altitude. Alternatively, a height of almost 800 km is reachable for 2100 kg total mass.

km, 3 days at the equator, and 1 K. The respective goal requirements were 10 km × 10 km, 1 day, and 0.5 K. The accuracy requirement reflects the performance after in-flight calibration and possible data aggregation, e.g. for measurements in an angular bin for multi-angular measurement systems.

The three-hexagon mission concept, or TriHex, is making an important step towards addressing the needs of a wide user community, particularly the goal requirement of 10 km ×10 km spatial resolution. TriHex is the result of the developments and reasoning explained in the previous sections, which can be summarized as the combination of:
1) A targeted spatial resolution of 20 km, which should satisfy more than 80% of the user community applications, at threshold level (see Fig. 5).
2) The use of formation flying.
3) The use of natural General Circular Orbits.
4) The use of alias-free imaging (0.577λ antenna spacing).
5) All lessons learnt from SMOS.
6) The choice of the simplest configuration possible.

The next paragraphs describe different aspects of TriHex mission concept in more detail.

A. Overall Description

TriHex consists of three hexagonal spacecraft of about 3 m of envelope diameter and 0.8 m in height, flying in formation, with their center of mass positioned at the vertices of a 5 m side equilateral triangle (Fig. 6, left top). The center of the triangle is a virtual point that follows the desired reference orbit of the constellation. The spacecraft keep their relative distance and orientation constant over time, except during the manoeuvres to go-to and return-from the Cold Sky pointing mode, used for calibration.

The three centers of mass of the three hexagons are in GCOs so that they follow the same circular trajectory in the plane of the triangle, spaced by 120°. The plane forms a roll angle of 30° with respect to the velocity vector (Fig. 6, right top), so that the boresight direction is at the same angle of 30° from nadir. The sense of the roll angle of the constellation is such that the backside of the spacecraft is oriented towards the Sun (Fig. 6, left bottom), a similar geometry to that of Aquarius [18]. This is convenient to mount solar cells at the back of the satellites, avoiding deployable moving solar panels which might perturb the position of the centers of mass, critical in the definition of the geometry of the formation. The estimated average power consumption of each spacecraft is of 750 W, provided by body mounted solar cells.

The antenna elements of the payload are disposed near the rim of each hexagon to maximize the final aperture (Fig. 6, right bottom). There are 12 elements on each side of the hexagon, i.e. 72 receivers in total. The final aperture achieved is near 9 m (Fig. 3).

The relative position is continuously provided by three GNSS antennas at the back of the satellites connected to a GNSS receiver (Fig. 6, left bottom), and controlled through a set of thrusters located in the center of each spacecraft. Two sets of three thrusters oriented along three orthogonal axes, with the main diagonal normal to the hexagon, are placed in the center of the front and backsides of the hexagons. Such disposition minimizes the impact of the plume of the thrusters between
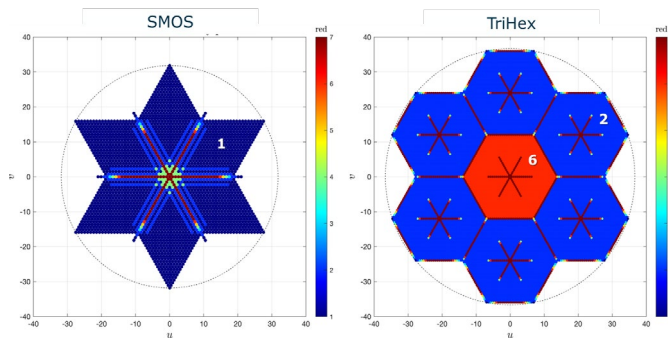
Fig. 9. Visibility coverage and degree of redundancy of SMOS (left) and TriHex (right). Axes span ±40 units in both u and v coordinates.

Fig. 10. Cuts, in director cosine coordinates, of the impulse response of SMOS (left) and TriHex (right). TriHex sidelobes along the ξ=0 plane (blue line) are around 3 dB lower than those of SMOS; and those along the η=0 plane (red line) have at least 5 dB lower amplitude. Horizontal axis spans ±1, vertical axis spans from 0 dB down to –40 dB.

spacecraft and other satellite subsystems.

The three hexagons of TriHex fit inside the fairing of a launcher like VEGA [19] (Fig. 7, left). They can be stacked one on top of the other through an adequate clamp-band separation system, in an approach similar to that employed for the ESA's Cluster mission. The satellites can then be readily released from the launcher (Fig. 7, right).

The estimated mass of each hexagon is of about 700 kg, and hence, the total mass of the three spacecraft is of 2100 kg. As explained later, the orbital height of TriHex is proposed to be around 500 km for best spatial resolution, and hence, according to Fig. 8, there is ample margin of performance for a VEGA-C launcher. There is also a comfortable margin in the height of the center of mass which, for a payload of 2100 kg, is limited to about 2.6 m. Being each spacecraft of about 0.8 m in height, and accounting for a 0.30 m gap for the interface between them, the center of mass is expected to be at a height near 1.8 m, well within the limit for VEGA-C.

B. UV-coverage, sidelobe level and angular resolution

The uv-coverage in the visibility domain of TriHex is shown in Fig. 9 (right). It consists of one central hexagon surrounded by other six. The degree of redundancy (number of measurements corresponding to one particular baseline) of the central hexagon is 6, and that of the surrounding hexagons is 2. The degree of redundancy of TriHex is greater than that of SMOS, which uv-coverage is also presented in Fig. 9 (left) for comparison. SMOS has redundancy 1 in the petals of the star, i.e. for all uv-points, except those along the diameters and a couple of lines parallel to those. This means that TriHex is more robust against the failure of receivers: at least 2 receivers have to fail before losing one particular visibility sample in the surrounding hexagons of the uv-coverage, and at least 6 receivers have to fail before one visibility is lost of the central hexagon. In SMOS the failure of 1 receiver already leads to the loss of visibility samples.

Another important feature of the degree of redundancy in TriHex is that the central hexagon has a high degree number (6), which leads to an improved radiometric resolution in the measurement of the central baselines which are the most energetic, hence expecting high quality images.

Although the envelope of the uv-coverage of TriHex is not a convex polygon as that resulting from a single hexagonal array,
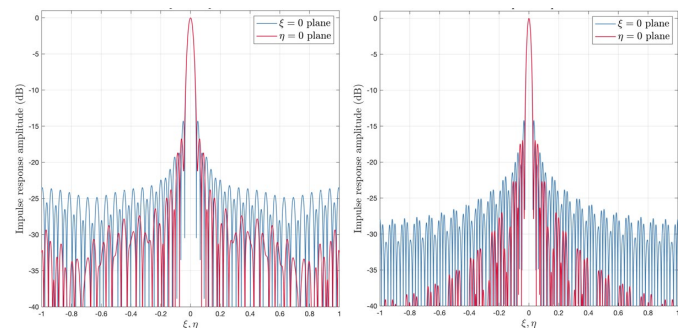
it approaches convexity more than that of SMOS. A metric to measure this closeness could be the area between the uv-coverage and the circumscribed circumference: the smaller the area the better the convexity. From Fig. 9 it is clear that the uv-coverage of TriHex is more convex than that of SMOS. Earlier studies, as in [4] and [20], concluded that the higher the convexity of the uv-coverage, the lower the sidelobes of the corresponding impulse response. This is confirmed in Fig. 10 and 11 where the sidelobes and noise floor of TriHex (right plots), apodized with a Hamming window, are compared against those of SMOS (left plots), weighed with Blackman. The tails of sidelobes of TriHex are 3 and 5 dB lower than those of SMOS in the main planes, and the noise floor is about 10 dB smaller. Lower sidelobes are important to mitigate the tails generated by bright points like those produced by RFI sources. redfocus the RFI energy and provide cleaner images than SMOS in the presence of interference.

Sidelobe level also plays an important role in the so-called land-sea contamination, observed in SMOS. Sidelobe level is determined by the geometry of the array (as explained) and the apodization window. SMOS sidelobes are relatively high due to the Y-shape of the array, causing brightness temperature errors along coastlines due to the contamination through sidelobe leakage (the sea looks warmer while the land looks colder than they should be). With its lower sidelobes, TriHex should observe less land-sea contamination.

The angular resolution of SMOS is determined with the Blackman window applied to the uv-coverage. As shown in Fig. 12 (left), this apodization reduces the first sidelobe of the impulse response from about 8.4 dB below the peak (when no window is applied) to some 14 dB. In TriHex, the angular resolution is established using the Hamming window instead, to maximize spatial resolution while maintaining better beam efficiency. This is because the application of the Hamming window to the TriHex uv-coverage leads to an impulse response having its first sidelobe of the same amplitude as that of SMOS (Fig. 12, right), the rest of the lobes having lower values (Fig. 11).

The resulting angular resolution of TriHex is 1.5°, as shown in Fig.12 (right), to be compared against 2.3° of SMOS (Fig. 12 left). The better angular resolution of TriHex comes from its
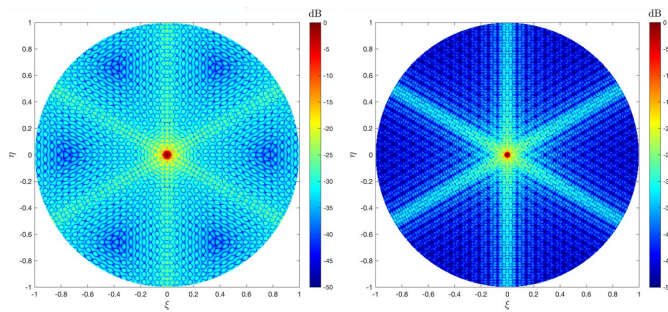
Fig. 11. Full impulse response of SMOS (left) and TriHex (right). The noise floor amplitude of TriHex response (level of sidelobes in between tails) is about 10 dB lower that of SMOS. Axes span ±1 in both ξ and η coordinates. Colour scales ranges from 0 dB (red) down to −50 dB (dark blue).
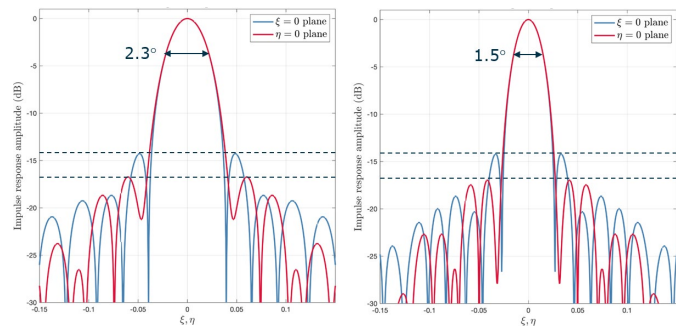

Fig. 12. First sidelobe level and angular resolution of SMOS (left) and TriHex (right). SMOS visibilities are apodised with the Blackman window while TriHex visibilities are affected by the Hamming window. The different apodisation achieves the same level for the first sidelobe in both cases.

larger aperture size (9 m against 8 m about), its better filling of the uv-plane and the lower sidelobe level of its impulse response that allows the use of less aggressive apodisation (Hamming window instead of Blackman).

C. Field of View, Range of Incidence Angles and Swath

Fig. 13 shows the field of view of SMOS in director cosine coordinates, as reference. In these coordinates, the boresight direction (BS) is at (0,0). Due to SMOS' 32.5° pitch angle, the nadir direction (NAD) corresponds to (−0.54, 0), and the Earth limb appears flattened towards the bottom of the unit circle of physical directions. The element spacing of SMOS, 0.875λ, causes the processing hexagon (set of directions where SMOS forms an image) to be smaller than the unit circle, and repetition of this hexagon (by translation) generates alias images (grating lobes) of the Earth and Sky. Only a small region of the unit circle is free of any aliases, the Alias-Free Field of View (AF-FoV). It is in this area where SMOS observations are the most accurate. Around the AF-FoV there is another part of the unit circle in which there are only one or two Sky aliases. In this region SMOS also provides useful observations, although less accurate, as they include corrections for the aliases of the unit border and the Sky.

Within the AF-FoV of Fig. 13 are shown three dwell lines, i.e. the path a point on ground traverses the field of view of the instrument as this moves along its orbit. The central dwell line is the one going through boresight (BS) and nadir (NAD), corresponding to the satellite ground track. The other two dwell lines are for points 300 km either side of the ground track. The incidence angle range over the central dwell line is of about 40°, obtained by reading the iso-incidence lines, shown in Fig. 13, that it traverses (removing a margin from the alias of the border of the unit circle). This range of incidence angle allows to retrieve the geophysical parameters with good accuracy. However, the other two dwell lines have a reduced incidence range, of only about 15°, which makes the geophysical retrieval less accurate.

Fig. 14 summarizes the range of incidence angles of SMOS (blue line) as a function of the cross track distance of the dwell line. The swath of SMOS within which the range of incidence angles is at least 10° is of about 650 km.

Similarly, the field of view of TriHex is presented in Fig. 15 for an orbital altitude of 500 km (the other orbital parameters corresponding to a Sun Synchronous Orbit with a Local Time of Ascending Node of 6 am, as SMOS). The orbital altitude of TriHex is lower than that of SMOS (775 km) in order to achieve high resolution on ground. Now the processing hexagon circumscribes the unit circle of physical directions and hence, no aliases are formed. This happens by design, as the inter-element distance in TriHex is precisely the alias-free spacing, that is, 0.577λ. Because TriHex has a roll angle of 30°, the nadir point (NAD) appears at (0, 0.5) in director cosine coordinates, and the Earth contour is flattened against the right of the unit circle.

The same dwell lines as in the case of SMOS are illustrated on Fig. 15, plus two additional ones 600 km on either side of the satellite ground track. The range of incidence angles as a function of the distance of the dwell lines to the satellite track can be determined as before and is shown in Fig.14 (red line). The swath of TriHex, using the same criterion as for SMOS, is now 900 km. The swath of TriHex is therefore substantially larger than that of SMOS, despite of flying at a significantly lower orbital height. This is possible after having enlarged the field of view of the instrument to the whole unit circle, i.e. getting rid of any limitation due to alias boundaries, as is the case of SMOS.

Moreover, TriHex does still collect observations, over a range of incidence angles equal to its angular resolution of 1.5°, 600 km on either side of the satellite ground track (Fig. 14). This corresponds to a total swath of 1200 km, to be compared against 800 km about total swath for SMOS. Although 1.5° is essentially a single angle, not suited for good retrievals in some applications, for others, it may well suffice.

It is further noticed in Fig.15 that TriHex can observe very high incidence angles, of 60° and beyond. It is here clarified that such capability is a result of the technical implementation, rather than sought from any requirement coming from the scientists. The future will tell what the scientific exploitation of those observations can deliver.
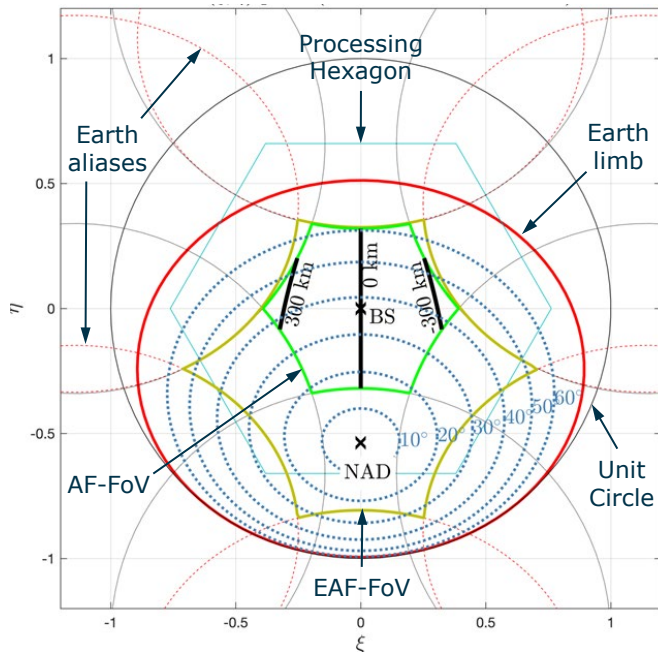
Fig. 13. SMOS field of view in director cosine coordinates, showing: the unit circle of physical directions, the Earth limb and its six aliases, the processing hexagon, the Alias-Free Field of View (AF-FoV), the Extended Alias-Free Field of View (EAF-FoV), the boresight (BS) and nadir (NAD) directions, some iso-incidence angle lines (from 0° till 60°), and three dwell lines at 0 km and ±300 km from the satellite track.
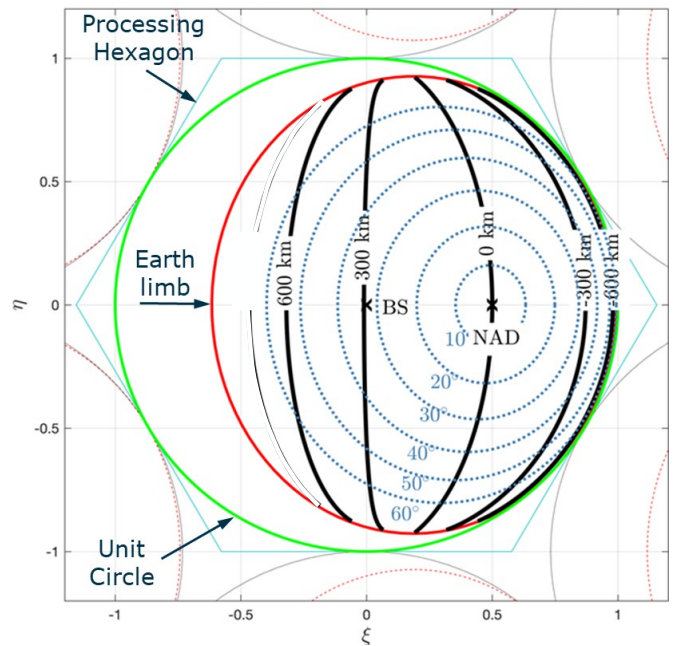

Fig. 15. TriHex field of view in director cosine coordinates, showing: the unit circle of physical directions, the Earth limb, the processing hexagon, the boresight (BS) and nadir (NAD) directions, some iso-incidence angle lines (from 0° till 60°), and three dwell lines at 0 km, ±300 km and ±600 km from the satellite track.
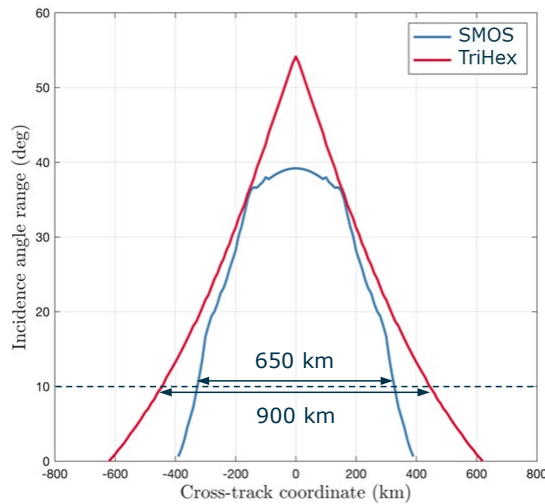

Fig. 14. Range of incidence angles as a function of the distance of the dwell line from the satellite track for SMOS (in blue) and TriHex (in red).

D. Spatial Resolution

Fig. 16 illustrates the field of view of SMOS, but this time in across-track, along-track coordinates. In these coordinates, it is the nadir point (NAD) which corresponds to the origin of coordinates, while the boresight point (BS) lies some 500 km ahead. The AF-FoV contour is shown. Its maximum width is about 800 km, as indicated. For reference, the iso-incidence line of 55° is drawn.

Fig.16 also provides the spatial resolution at nadir, 33 km, and the iso-spatial resolution lines for 40 and 50 km. The crossing points, A and B, between the 40 km iso-line and the AF-FoV contour, define the swath in which a spatial resolution of 40 km is achieved. Similarly, the swath at 50 km is defined by points C and D. Proceeding in this way, the swath as a function of spatial resolution for SMOS can be obtained, and is shown in Fig.17 (blue line).

Fig. 18 presents the same information as Fig. 16 but for TriHex. All iso-lines extend less because TriHex altitude is lower than that of SMOS. For the same reason one can now see the 20 and 30 km iso-lines which were not appearing in Fig. 16. The spatial resolution of TriHex at nadir (NAD) is 15 km, much better than the 33 km of SMOS. Because TriHex is alias-free, the swath for a given spatial resolution extends the diameter of the corresponding iso-line. For example, the swath, defined by the distance from C to D (1400 km), at 50 km spatial resolution, is much larger than in the case of SMOS (800 km), and the swath at 40 km is of about 1200 km. The swath as a function of spatial resolution is shown in Fig. 17 (red line). The much larger swath realized by TriHex in comparison to that of SMOS is apparent. Furthermore, from Fig. 17 one can deduce that TriHex provides a swath of 200 km at 15 km spatial resolution and a swath of 600 km at 20 km.

Another useful plot is presented in Fig.19, which shows the spatial resolution as a function of the angle of incidence along the dwell lines, for both SMOS and TriHex. Each line in Fig.19 corresponds to a dwell line at a specific across-track distance (100 km spacing in the case of TriHex), so that the range of
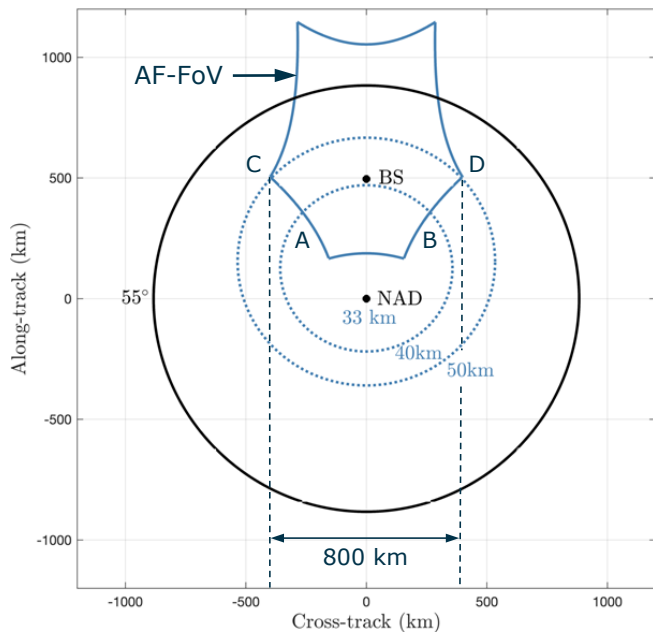
Fig. 16. SMOS field of view in across-track, along-track coordinates, showing: the Alias-Free Field of View (AF-FoV) and its corresponding total swath, the line of 55° incidence angle, some lines of iso-spatial resolution, and the boresight (BS) and nadir (NAD) directions.
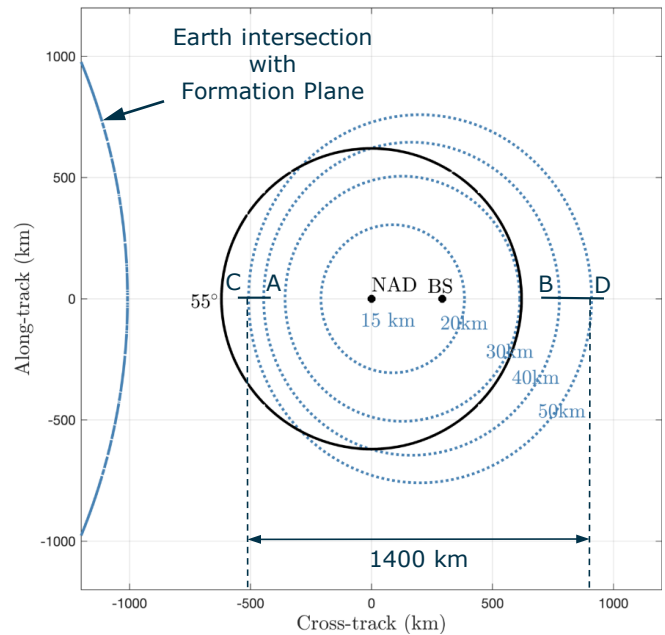

Fig. 18. TriHex field of view in across-track, along-track coordinates, showing: the iso-spatial resolution lines, including the ones at 20 and 30 km, the line of 55° incidence angle, and the boresight (BS) and nadir (NAD) directions. As TriHex is alias-free, there is no Alias-Free Field of View line.
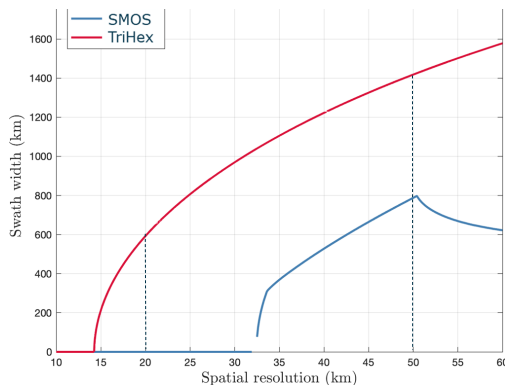

Fig. 17. Swath at which a given spatial resolution is attained for SMOS (blue line) and TriHex (red line).

incidence angle, those of TriHex are observed in both directions, that is, from the larger to the smaller incidence angle and then back to the larger incidence angle. This is a consequence of the alias-free condition of TriHex and the limited view of the dwell lines in SMOS, constrained by the alias-free region. Tracing the dwell lines in opposite directions gives TriHex the potential of exploring directional features of the surface emissivity

Fig. 19 also shows that the swath of TriHex is not symmetric with respect to the satellite track as it is that of SMOS, but it is shifted to the side the formation is rolled. Assuming a minimum range of incidence angles of 10° is required at the edges of the swath to provide good geophysical retrievals, then, from Fig. 19, one can deduce the swath widths TriHex can provide as a function of spatial resolution. Some are collected in Table I.

incidence angles as well as the spatial resolution along them is provided in this plot. For example, the dwell line along the satellite track in SMOS starts at an incidence angle of about 15° with a spatial resolution of 33 km and ends at 60° with 80 km. Instead, in the case of TriHex, the same dwell line starts at 0° with 14 km and ends at 70° with 80 km, having a spatial resolution of 50 km at 60°. Therefore TriHex improves both the spatial resolution as well as the range of incidence angles of this dwell line significantly. The same occurs for other dwell lines: for the one at +300 km, SMOS starts at 37°, 43 km, ending at 54°, 64 km, while TriHex starts at 33°, 17 km, reaching 32 km at 54°; the dwell line at −300 km is identical to the one at +300 km in the case of SMOS, while TriHex starts it at 33°, 25 km, reaching 48 km at 54°.

It is important to note that while SMOS dwell lines are traversed only in one sense, from the larger to the smaller

TABLE I
TRIHEX SWATH WIDTH VERSUS SPATIAL RESOLUTION,
ENSURING A MINIMUM RANGE OF INCIDENCE ANGLES OF 10°

Spatial Resolution	Swath	Near Limit (cross track)	Far Limit (cross track)
< 17 km	200 km	−50 km	+150 km
< 20 km	400 km	−150 km	+250 km
< 30 km	700 km	−275 km	+425 km
< 40 km	875 km	−350 km	+525 km
< 50 km	1025 km	−400 km	+625 km

E. Radiometric Resolution

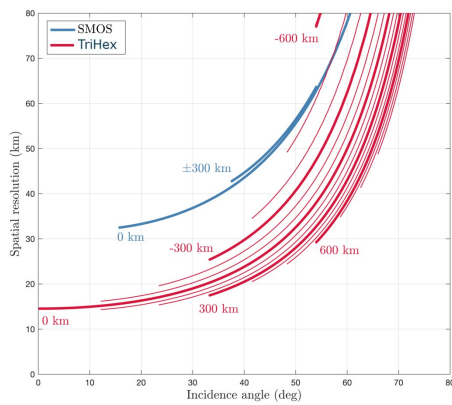Fig. 20 shows the radiometric resolution of SMOS over the

Fig. 19. Spatial resolution as a function of incidence angle for various dwell lines for SMOS (blue lines) and TriHex (red lines, 100 km spacing).
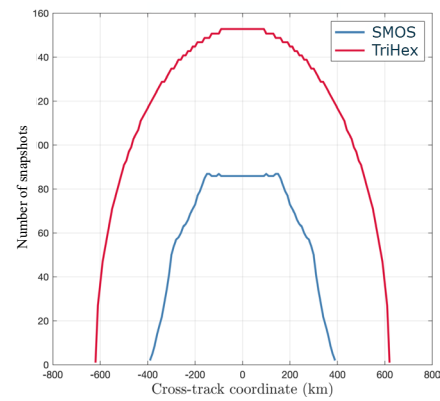

Fig. 21. Number of snapshots taken per dwell line as a function of its distance to the satellite ground track for SMOS (in blue) and TriHex (in red).
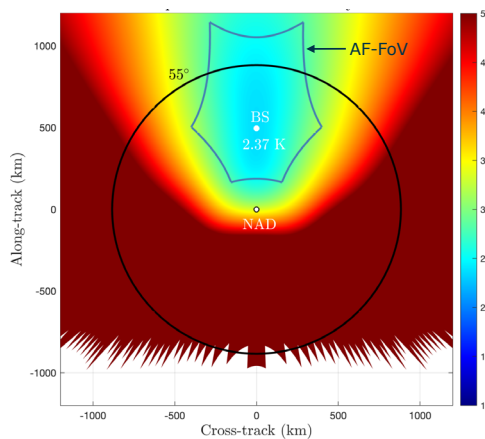

Fig. 20. Radiometric resolution of SMOS over the field of view for a uniform 150 K scene.
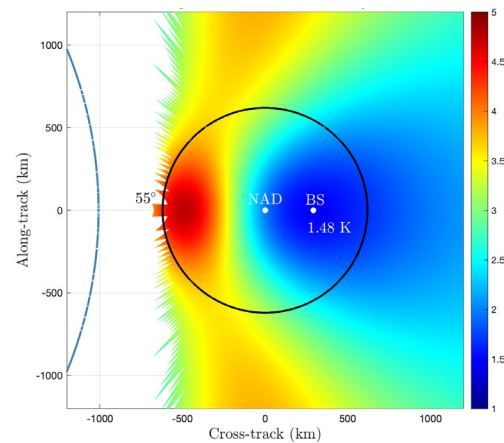

Fig. 22. Radiometric resolution of TriHex over the field of view for a uniform 150 K scene.

field of view, in across-track, along-track coordinates, for every 1.2 s snapshot. The radiometric resolution, for a flat scene of 150 K, is of 2.37 K at boresight, and degrades quite rapidly due to the roll-off of the antenna patterns, reaching 3 K near the Alias-Free Field of View (AF-FoV) contour. The snapshot sensitivity is that corresponding to each of the 1.2 s observations performed along a dwell line. The closer a dwell line is to the satellite ground track, the longer it is observed, and the more snapshots are taken. Fig. 21 (blue line) gives the number of snapshots that SMOS takes along a particular dwell line, up to 55° incidence angle, as a function of its across-track distance. For example, for the dwell line along the satellite ground track, i.e. at 0 km across-track distance, there are about 86 snapshots taken. The accumulated integration time of all these snapshots is sequentially distributed between the vertical and horizontal polarizations in order to acquire the four Stokes parameters in the polarimetric mode of SMOS [21]. This means that 86/2=43 observations are taken of each polarization, resulting in an effective radiometric resolution of, roughly, the snapshot sensitivity at boresight divided by the square root of 43, that is, 0.36 K.

The radiometric resolution of TriHex over the field of view

for the same uniform scene at 150 K is presented in Fig. 22. The snapshot sensitivity at boresight is of 1.48 K, better than that of SMOS (2.37 K). There are six main reasons behind such improvement: (a) TriHex would measure the two polarizations simultaneously using an advanced L-band receiver [22], doubling the observation time; (b) the antenna polarization axes are aligned with those of each side of the hexagonal array [23], reducing losses in the combiner circuit connecting each antenna to its receiver; (c) a simpler lower loss 2:1 switch needed at the front-end, while a 4:1 switch was necessary in SMOS; (d) improvements in the antenna [24] and low noise amplifier [22] leveraging the technology progress over these years; (e) the higher degree of redundancy as earlier mentioned; and finally (f) being the antenna elements always in the dark side of the spacecraft, i.e. with no Sun illumination, it is possible to operate them at a lower physical temperature than in SMOS, which reduces receiver noise. All these improvements compensate, with margin, the following degradation factors: the increased number of baselines and the reduced dwell time over the smaller pixels on ground (due to the enhanced spatial resolution).

As it can be drawn by comparing Fig. 20 and Fig. 22, the radiometric resolution in TriHex degrades more gradually than
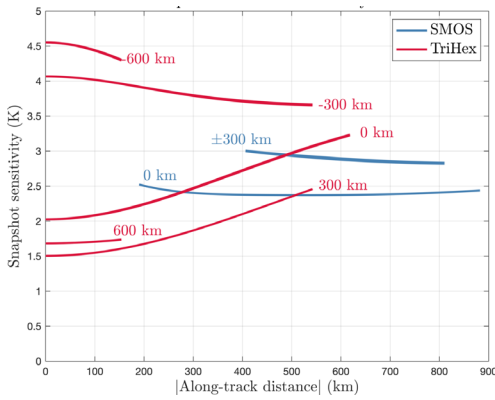
Fig. 23. 1.2 second snapshot sensitivity of TriHex and SMOS as a function of the along-track distance from nadir assuming a 150 K uniform Earth (note: for TriHex the plot gives also the performance for the mirrored negative along-track positions). Different lines correspond to dwell lines at different across-track positions.
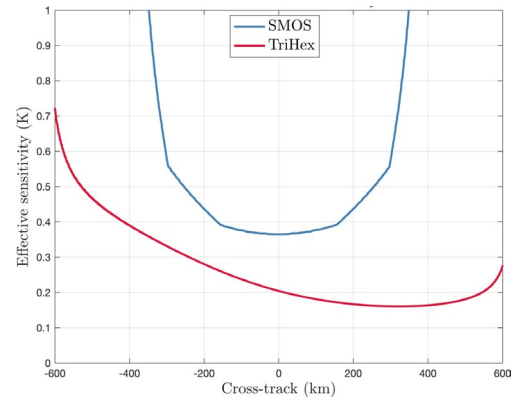

Fig. 24. Effective sensitivity of TriHex and SMOS as a function of cross-track from nadir assuming a 150 K uniform Earth.
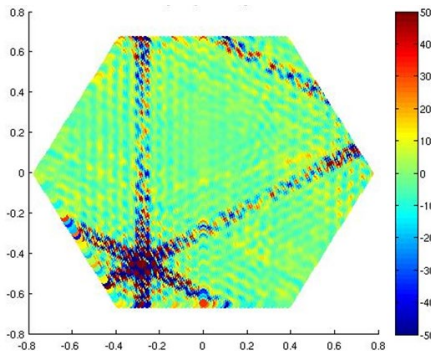

Fig. 25. Sun image acquired by SMOS during a Cold Sky calibration. The coordinates are the director cosines and the brightness temperature scale is in Kelvin. The tails of the instrument impulse response are clearly visible.
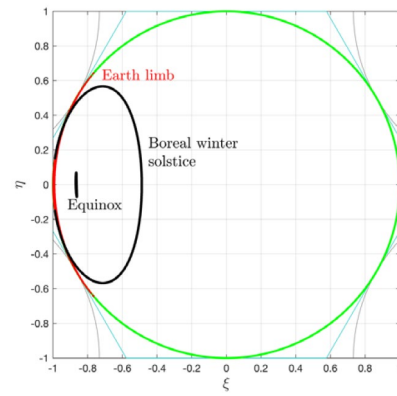

Fig. 26. Unit circle representing the rear hemisphere of TriHex and the trajectory followed by the Sun in one orbit during the boreal Winter solstice and during the equinox (black lines). A small portion of the Earth limb appears in red, which eclipses the Sun during a fraction of the orbit at the solstice.

in SMOS as one moves away from boresight. This happens because the smaller antennas of TriHex have broader patterns with smoother roll-off slopes. Due to this fact, TriHex radiometric resolution is always within 4.5 K inside the circle of 55° incidence angle, while SMOS radiometric resolution degrades to much larger values.

The number of snapshots TriHex can take along the dwell lines (up to 55° incidence angle) is also shown in Fig. 21 (red line). The values are much larger than those for SMOS because of its more extended field of view, and, since TriHex acquires the two polarizations in parallel, all snapshots contribute to improve the effective radiometric resolution per polarization. For the dwell line along the satellite track, TriHex collects about 152 snapshots, while only 86 were observed in the case of SMOS. This leads to an effective radiometric resolution of 0.20 K for TriHex, a factor 1.8 better than the corresponding 0.36 K in SMOS.

As a summary, Figures 23 and 24 present the 1.2 second snapshot and the dwell-time effective sensitivities, respectively, of both, TriHex and SMOS. The snapshot sensitivity in Fig. 23 is given as a function of the along-track distance from nadir, for several dwell lines at different across-track positions (note that the TriHex curves also provide the sensitivity values for negative along-track positions, by symmetry). SMOS snapshot sensitivity is between 2.4 and 3.0 K over a swath of 600 km, while TriHex snapshot sensitivity is between 1.5 and 4.5 K over a swath of 1200 km. The TriHex snapshot sensitivity is generally better than that of SMOS for positive across-track dwell lines, and worse for negative ones. But despite of this, the effective sensitivity of TriHex is significantly better than that of SMOS as Fig. 24 demonstrates. For example, for the dwell line of +300 km, SMOS average snapshot sensitivity is about 2.9 K (Fig.23) and takes 50 observations (Fig. 21), 25 per polarization, yielding an effective radiometric resolution of 0.58 K. For the same dwell line, TriHex attains an average snapshot sensitivity of 2.5 K over 134 observations. This corresponds to 0.17 K effective radiometric resolution, a factor 3.4 improvement with respect to SMOS (0.58 K). For the −300 km dwell line, the average radiometric sensitivity is 3.8 K, and the corresponding effective averaged sensitivity 0.33 K, which is still better than that of SMOS (0.58 K).

It is worth noting that TriHex effective sensitivity is better than the best value of SMOS (0.33 K attained at the 0 km dwell line) over a swath of 900 km (from −300 to +600 km across-
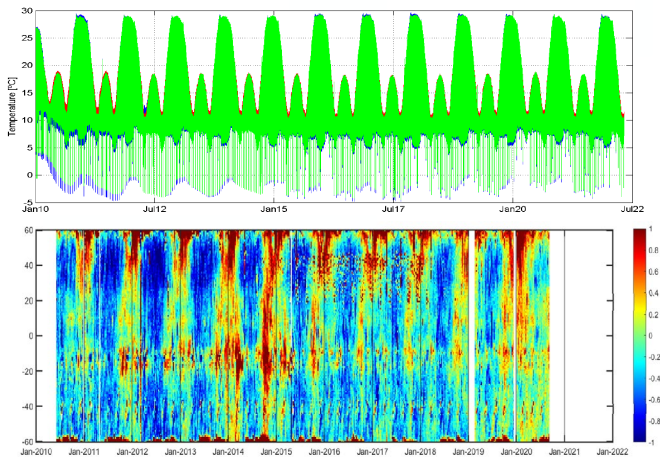
Fig. 27. Physical temperature of the antennas in SMOS during the completed mission duration (top figure). The pattern exhibits local maxima at the solstices. The one during the boreal winter has an amplitude of about 20°C. These maxima cause a repeated error pattern in the Hovmoller plot of the brightness temperature error map over the ocean, as it is apparent in the bottom figure (colour scales is in Kelvin).

track dwell lines). In other words, the radiometric sensitivity does not restrict the swath of TriHex.

F. Sun Interference and Eclipse Effects

Sun interference and eclipse effects are two sources of image errors in SMOS. Sun interference refers to the contamination of the image by the side lobes of the Sun while eclipse effects are produced by the rapid change of the physical temperature of the antenna when SMOS enters or exits the Earth's umbra. Both mechanisms are fully eliminated in TriHex because its roll angle of 30°, which makes the Sun to be situated always at the back of the array, all along the orbit, all days of the year. This is another major step forward of TriHex with respect to SMOS, leaning on all lessons learnt from the latter.

The Sun interference is illustrated in Fig. 25 which shows the tails of the impulse response of the MIRAS instrument excited by the presence of the Sun. The tails cross the processing hexagon from side to side. Although Fig. 25 is a worst case as the Sun was imaged with the instrument pointing towards the Cold Sky, it exemplifies the error propagation due to the presence of the Sun in front of the instrument. The geometry of the Sun synchronous orbit of SMOS is such that the Sun revolves around the normal to the orbital plane once per orbit, at an angle that changes throughout the year, with two local maxima at about 15° and 31° at the solstices. Given the orientation of the SMOS antenna, this causes the Sun to be in front of the array during half of every orbit, and behind, during the other half. The images produced in the half orbit when the Sun is in front of the array can be affected by the Sun tails. This is a problem that never happens in TriHex because the Sun remains always at the back of the array as shown in Fig. 26.

Fig. 27 (top) shows the physical temperature of the antenna of SMOS over the mission duration. During the solstices the orbital excursion of the physical temperature is the largest because the Sun reaches the highest elevation over the antenna

plane. In addition, during the boreal winter, the Sun is eclipsed by the Earth when SMOS flies in the most northern latitudes. At the start of the eclipse, the physical temperature of the antenna drops from around 30°C down to 5°C, a 25°C rapid variation which affects the measurements of the brightness temperature and is difficult to correct. An opposite rise occurs at the end of the eclipse. The effect of these fast temperature variations on instrument accuracy can be seen when comparing the measured brightness temperature over the ocean with modelled values. This deviation is presented in the Hovmoller plot of Fig. 27 (bottom). A repeated pattern of warmer temperatures than expected, of an amplitude reaching about 1 K, happens every boreal winter [25]. This error pattern is not to happen in TriHex because the Sun is always behind the antenna plane, and the Sun eclipse happens also in the rear hemisphere (Fig. 26). The physical temperature of the antennas is therefore expected to be far more stable than the top plot in Fig. 27.

Furthermore, the thermal control of TriHex could be designed to have the receivers operating at an average antenna physical temperature of 5°C, for example, and very little variation would happen along the orbit and the year. As mentioned earlier, this temperature, lower than the operating temperature of SMOS (around 22°C), would allow the receivers to exhibit a better noise figure. The measured noise figure of SMOS is 2.21 dB while that for TriHex is 1.38 dB (estimated from measurements [22]).

In summary, by having the Sun always on the back of the array, TriHex would avoid completely two of the main issues found in SMOS: the Sun interference and the eclipse effects, achieving better accuracy and stability.

G. On Antenna Coupling, Image Processing and Calibration

The distance between antenna elements in SMOS is 0.875λ, and the coupling factor between closest elements was measured to be lower than -30 dB [26]. In TriHex, as explained earlier, the antenna spacing is reduced to 0.577λ to achieve alias-free conditions. This shorter spacing is expected to produce higher mutual coupling, of the order of -20 dB according to simulations [24], i.e. some 10 dB larger than in SMOS. The question arises what effect this higher coupling might have in the images of TriHex.

The coupling factor between antenna elements translates into a modification of the antenna pattern of the isolated elements, which yields the final embedded patterns [27]. As done in SMOS, the embedded patterns of TriHex are to be accurately measured in an antenna test range, and then stored for use in the image processing.

The image processing of TriHex is very similar to that of SMOS, as both share the same hexagonal sampling of the visibility function and first principles. The processing is based on the Corbella equation [28], a fundamental variation of the van Cittert-Zernike theorem that conceals it with the Bosma theorem [29].

There are two main differences in the processing of TriHex by comparison to that of SMOS. The first one is the need to account for the true relative position between phase centers of elements belonging to different spacecraft. The control in the
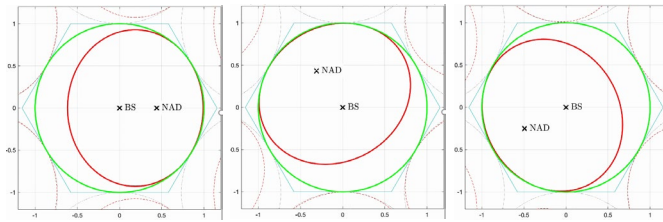
Fig. 28. Earth limb as seen within the unit circle in three acquisitions spaced by one third of the orbital period. The image processing can take this rotation into account as well as that of the Earth.
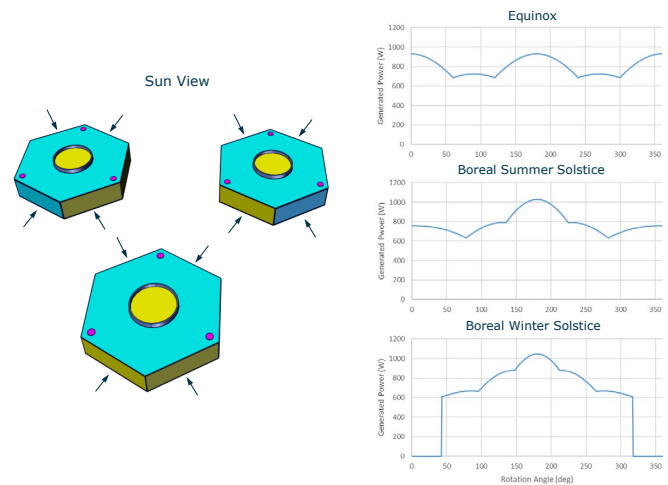

Fig. 29. Generated power as a function of time during the equinoxes (top right), the boreal Summer solstice (middle right) and the boreal Winter solstice, including the eclipse (bottom right). Body mounted cells are assumed on the surface of the hexagon (excluding the circle at the center) and on the four lateral panels indicated with the arrows.

relative positioning between the three hexagons is expected to achieve 5 mm [11], while the knowledge of the baselines can be of the order of 1mm using GNSS carrier phase based relative navigation.

The second difference in the processing of TriHex stems from the fact that the three hexagons rotate in the constellation plane once per orbit, maintaining their relative orientation. This is effectively as if the boresight of the full synthetic array rotated at the same angular rate. Equivalently, for a non-rotating observer sitting at the center of the constellation, the scene turns around in the field of view at the orbital period (Fig. 28). The data processor can easily handle this turning of the scene as well as that coming from the Earth rotation through the appropriate transformation from antenna director cosines to pixel latitude-longitude coordinates. Nonetheless, the data processor could be made to display images in the format shown on the left plot of Fig. 28, as this is the familiar format used in SMOS.

It is also noted that, to enhance the range of incidence angles at the edge of the Alias-Free Field of View, SMOS performs a yaw-steering that corrects for the Earth rotation effect on the dwell line. In TriHex this approach is not needed as there are no aliases. It is also not practical because that would require to introduce an angular acceleration in the motion of the three centers of mass of the formation along their relative circular trajectory, leading to an unnecessary expenditure of propellant.

The calibration approach of TriHex also follows that of SMOS. It is based on a mixture of internal calibration by noise injection, and external calibration using the Cold Sky. The manoeuver to turn the formation to point to the Cold Sky is still to be developed in detail, but it will be the same strategy as in [30]. The Cold Sky view allows TriHex to get its Flat Target Response to accurately calibrate all its observations through the application of the Flat Target Transformation [31]. For the reasons given in the next section, the Cold Sky calibration of the TriHex formation can only be achieved around the boreal Winter solstice. However, there is the possibility of performing Cold Sky calibrations of the individual hexagons, these not being constrained to happen around the solstice.

In summary, although TriHex antenna elements will have higher mutual coupling due to its closer spacing, the application of the techniques developed within the SMOS project for image processing and instrument calibration are expected to result in a successful outcome.

H. Solar Illumination and Solar Panels Concept

TriHex relies on the General Circular Orbits which are followed by the center of mass of the three hexagons. Therefore, the position of the center of mass of each spacecraft becomes critical in the TriHex mission concept. The spacecraft have to be designed to have their center of mass at a precise position, and to minimize their variation due to any mass loss or any internal movement of mass. This aspect, when it comes to power generation, calls for avoiding, if possible, any deployable solar panel and, even more, a rotating panel. For this reason and, given the fact that the Sun is always behind the hexagons of the TriHex formation, the use of body mounted solar cells is proposed.

A check of the available surface and the power that could be generated has been carried out. Assuming a total end-of-life efficiency of about 20% (hence, an availability of 271 W per square meter of solar cells), the generated power as a function of the rotation angle of the hexagons (or, equivalently, time) has been found and is represented in Fig. 29. It has been assumed that the complete surface of the back of the hexagon, except for the circle at its center, is covered with cells, as well as four out of the six lateral panels (those four panels indicated with arrows in Fig. 29). The power over rotation angle has been found taking into account that an observer sitting on the plane of the constellation, on the side of the Sun, will see the hexagons rotating counter-clockwise around him, and the Sun following an apparent circular motion around the orbit normal in the clockwise direction (Fig. 30). The phase of the formation within its rotation plane is designed to have the equilateral triangle defined by the centers of mass with its lower vertex at the plane defined by its rotation axis and the orbit normal at the time the Sun is at its lowest elevation above the formation plane. Taking the intersection line between those two planes (formation plane and plane defined by rotation axis and orbit normal) as origin of the rotation angle, three cases are analyzed: the equinox, the
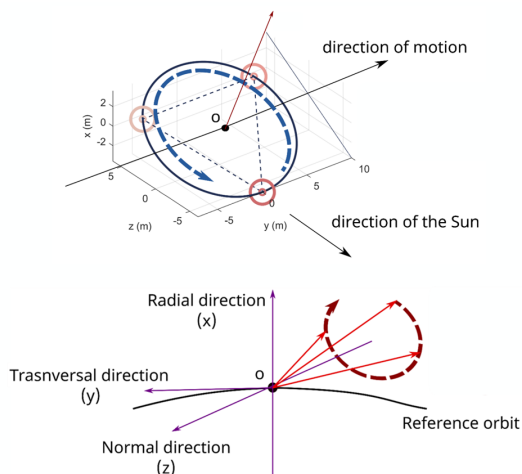
Fig. 30. Direction of rotation, counter-clockwise, of the hexagons in the plane of their relative circular trajectory (top), and direction of the apparent rotation of the Sun around the negative orbit normal, clockwise (bottom).

boreal Summer solstice and the boreal Winter solstice (refer to Fig. 29).

During the equinox, the orbital average available power is 801 W and during the boreal Summer solstice 784 W. In the boreal Winter solstice, the Earth eclipses the Sun for a maximum duration of 23.5% of the orbital period (about 22 minutes). This worst case, presented in Fig. 29, results in an orbital average power of 603 W. Therefore, the yearly average power that can be generated from body mounted cells is around 750 W. This number can be trimmed by extending the height of the hexagons. For example, increasing the height from the current 0.8 m to 1 m would provide 90 W of additional power.

Fig. 29 also shows that the peaks of the generated power occur during the solstices, when the Sun is at about its highest elevation angle above the formation plane. The peak power is about 1050 W. Those are the best moments to initiate Cold Sky manoeuvers because the generated power can feed the electrical propulsion thrusters. However, the Cold Sky acquisitions can be planned only around the boreal winter, between October 25th and February 16th, when the Sun is at an elevation angle of below 10°. SMOS performs the Warm calibrations in the same way [32].

I. Some Technical Features

The technology of TriHex is mostly based on the one used in SMOS, improved through technology activities ESA is, or has been, carrying out [33]: a 0.577λ envelope antenna [24], a dual-frequency advanced receiver [22] including a new RF ASIC [34], a multi-wavelength optical harness [35] and an advanced correlator unit with the built-in capability of filtering out Radio Frequency Interference [36].

An important novelty of TriHex is the formation flying at close range. The relative position is to be obtained from GNSS carrier phase based real time relative positioning. For this purpose three antennas (visible in the Sun view of Fig.27) are connected to a GNSS receiver on each spacecraft, and the measurements are shared over an RF link. The control of the relative positioning is to be achieved through electrical propulsion thrusters.

The interferometric joint operation requires the three arrays to be syntonized and synchronized. TriHex relies on the Upper Side Band Syntonization (USBS) concept described for two spacecraft in [37] but extended to N=3 spacecraft [38]. The USBS concept was successfully demonstrated in the ESTEC RF Laboratory [39]. For synchronization TriHex relies on spatial symmetry, in practice realized by (a) manufacturing identical circuits with phase similarity to within 117° at 250 MHz, (b) cutting optical fibres with 3-millimetre accuracy and (c) having the spacecraft in relative navigation with an accuracy of 1 cm. These are achievable specifications that will guarantee 1.3 ns level synchronization, more than enough to match the 52.6 ns coherence time of the 19 MHz filtered radiation.

Spacecraft A performs the correlations of all its baselines (A-A), and those with the previous hexagon (C-A); spacecraft B performs B-B and A-B, and spacecraft C, C-C and B-C. To make this possible every hexagon sends all its raw measurements to the next hexagon using multiple laser links. The laser links are implemented for each of the 72 fibres coming out from the receivers in three sections: a single-mode transmitting fibre, a lens system, and a multi-mode receiving fibre. As it was done for SMOS, optical fibre spools are to be employed to equalise the different path lengths from a given correlator unit to remote and local receivers.

TriHex internal calibration through noise injection follows the same strategy as the overlapped distribution trees of the Calibration System of SMOS [40] across the three spacecraft, while a centralized approach is adopted within each hexagon. For the overlapped part, the output of a noise source in satellite B is converted to optical and sent to satellites C and A. Then the CA baselines can be calibrated. The same for the other two satellite pairs. The coherence of the noise injection is ensured by the spatial symmetry (cutting these optical fibres to 1 mm accuracy) and the tight relative positioning control between the spacecraft (< 1 cm).

Every spacecraft has all the necessary equipment for telemetry, telecommand and data downlink.

In summary the three TriHex spacecraft are identical and are operated in a way to function as a single array.

VI. CONCLUSION

Achieving high resolution in L-band passive observations remains, still today, a big challenge. SMOS and SMAP missions provide state-of-the-art 40 km resolution observations, despite having significantly surpassed their design life time. This paper has presented a novel mission concept, TriHex (short name for "3 hexagons"), which opens a new path towards achieving the user goal requirement of 10 km spatial resolution. A particular implementation of the concept has been described, consisting of 3 hexagonal spacecraft, without any deployable parts, which could be launched using a cost-effective launcher like VEGA-C. By combining formation flying, natural general circular orbits and alias-free imaging, it

is possible to reach a spatial resolution of better than 17 km over a 200 km swath. This mission concept, in turn, avoids the non-desired Sun effects found in SMOS because, thanks to its peculiar geometry, the Sun is always located behind the antenna plane. Moreover, the radiometric resolution of TriHex is expected to be considerably better by comparison to that of SMOS.

This new mission concept is flexible and fully scalable, given that the corresponding challenges are addressed: an hexagonal formation of double the number of satellites of TriHex (i.e. 6 satellites), or a formation like TriHex but with 3 larger spacecraft (for example, fitting the fairing of a larger launcher) would improve by a factor 2 the spatial resolutions of Table I. If realized, TriHex would become a milestone in passive remote sensing at L-band.

ACKNOWLEDGMENT

REFERENCES

[1] Kerr, Y., P. Waldteufel, J. P. Wigneron, J. M. Martinuzzi, J. Font, and M. Berger, 2001: Soil moisture retrieval from space: The soil moisture and ocean salinity mission (SMOS). IEEE Trans. Geosci. Remote Sens., 39, 1729–1735.

[2] J. Font, A. Camps, A. Borges, M. Martín-Neira, J. Boutin, N. Reul, Y. Kerr, A. Hahne, and S. Mecklenburg, "SMOS: The challenging measurement of sea surface salinity from space", Proceedings of the IEEE, vol. 98 , no. 5 , pp. 649–66, May 2010.

[3] M. Martín-Neira, Notes of the Operational SMOS session during the SMOS Workshop, Lisbon, 13-17 Sep. 2004.

[4] I. Corbella, F. Torres, N. Duffo and M. Vall-llossera, "Super-MIRAS: Analysis of Instrument Configurations", Rep. XMIR-UPC-DD-1C, Feb. 2011.

[5] A. M. Zurita, I. Corbella, M. Martín-Neira, M. A. Plaza, F. Torres and F. J. Benito, "Towards a SMOS Operational Mission: SMOSops-Hexagonal", IEEE Journal of Selected Topics in Applied Earth Observations and Remote Sensing, Vol. 6, No. 3, pp. 1769-1780, June 2013.

[6] "ECMWF/ESA workshop on using low frequency passive microwave measurements in research and operational applications", Rep. Summary, Reading, UK, 4-6 Dec. 2017.

[7] (a) Yann Kerr et al., "Low Frequency Passive Microwave User Requirement Consolidation Study: Requirement analysis for future systems, SO-TN-CB-GS-0075, Issue 2.2, date 09/09/2019.
(b) Yann Kerr et al., "Low Frequency Passive Microwave User Requirement Consolidation Study: Cluster Analysis Report, SO-TN-CB-GS-0082, Issue 2.0, date 09/10/2019.

[8] D. Entekhabi, E. G. Njoku, P. E. O'Neill, K. H. Kellogg, W. T. Crow, W. N. Edelstein, J. K. Entin, S. D. Goodman, T. J. Jackson, J. Johnson, J. Kimball, J. R. Piepmeier, R. D. Koster, N. Martin, K. C. McDonald, M. Moghaddam, S. Moran, R. Reichle, J. C. Shi, M. W. Spencer, S. W. Thurman, L. Tsang, and J. Van Zyl, The Soil Moisture Active Passive (SMAP) Mission, Proceedings of IEEE, Vol. 98,No. 5,pp. 704-716, May 2010.

[9] "The 2022 GCOS ECVs Requirements", Global Climate Observing System Report.

[10] M. Martín-Neira, R. Díez-García, A. Olea, A. Solana, J. Closa, A. Zurita, J. Herreros, M. García, A. García, I. Corbella, I. Durán, F. Torres, N. Duffo, "Low Side Lobe Level Image Reconstruction in Microwave Interferometry", MicroRad-2018, Massachusetts Institute of Technology, Cambridge (MA, USA), 27-30 March 2018.

[11] F. Scala, C. Colombo, B. Duesmann and M. Martín-Neira, "Natural relative trajectory design of satellites formation for remote sensing", submitted to the Astrodynamics Journal, currently under review.

[12] F. Scala, C. Colombo, B. Duesmann, and M. Martin-Neira, "Analysis and design of future multiple satellite formation flying L-band missions in low Earth orbit", Proceedings of the International Astronautical Congress, pp.1-12, Sept 2022.

[13] François Cabot, Eric Anterrieu, Thierry Amiot and Yann H. Kerr, "ULID: an unconnected L-band interferometer demonstrator", IGARSS-2019, Yokohama, Japan.

[14] Goutoule J.M and De Boer F,. "Large interferometer antennas synthesised by satellites formation for Earth remote sensing", IGARSS-2000 proceedings, Vol.2, pp. 869-870, Honolulu, Hawaii (USA).

[15] R. M. Mersereau, "The processing of hexagonally sampled two-dimensional signals", Proceedings of the IEEE, Vol.67, No.6, June 1979.

[16] R. Díez-García and M. Martín-Neira, "Antenna spacing and pattern differences: their impact in MIRAS reconstruction error", Proceedings of MicroRad 2016, Espoo, Finland, 11-14 April 2016.

[17] Anterrieu, E. and Yu, L. "Impactof the Antenna Spacing on the Brightness Temperature Maps Retrieved with a Synthetic Aperture Imaging Radiometer"", Remote Sensing 2023, 15, 805.

[18] LeVine, D. M., G. S. Lagerloef, and S. Torrusio. 2010. "Aquarius and Remote Sensing of Sea Surface Salinity from Space." Proc. IEEE 98 (5): 688-703 [10.1109/JPROC.2010.2040550].

[19] Arianespace, "VEGA C User's Manual", Issue 0, Revision 0, May 2018.

[20] Raúl Díez-García, "Side Lobes in SMOSops: Preliminary Investigations", Presentation at SMOS Payload Calibration Meeting, ESAC, Madrid, March 2017.

[21] M. Martin-Neira, S. Ribo and A. J. Martin-Polegre, "Polarimetric mode of MIRAS," in IEEE Transactions on Geoscience and Remote Sensing, vol. 40, no. 8, pp. 1755-1768, Aug. 2002, doi: 10.1109/TGRS.2002.802489.

[22] Roger Vilaseca, Albert Catalán, José Montero, Montserrat Puertolas, Bianca Santano, Dani Giménez, Ignasi Corbella, "Advanced Receiver for Future L-Band Radiometer development results", Proceedings of ESA's Living Planet Symposium, Bonn, Germany, 23-27 May 2022.

[23] M. Martín-Neira, M. Suess, E. Gandini, "On Antenna Polarization Axes in L-Band Aperture Synthesis Arrays With Dual Polarization Receivers for Earth Observation", IEEE Geoscience and Remote Sensing Letters, vol.19, pp.1-3, 2022.

[24] Q. Garcia-Garcia, D. Espinosa1, A. Zurita1, J. Closa1, E. Gandini, M. Suess, M. Martin-Neira, "Antenna Element Study for a Future SMOS Mission", Proceedings of the 16th European Conference on Antennas and Propagation, Madrid, Spain, 27-March 1-April 2022.

[25] R. Díez-García, R. Oliva, R. Crapolicchio, M. Martín-Neira, "SMOS v724 Third Mission Reprocessing: Brightness Temperature Quality and Stability", IEEE Transactions on Geoscience and Remote Sensing, Vol. 60, 2022.

[26] EADS-CASA Espacio, "MIRAS Demonstrator Pilot Project 2: Antenna Test Report", Report MPD2-CAS-3200-RPT-002, 17 October 2002.

[27] S. Blanch, J. Romeu, and I. Corbella, "Exact Representation of Antenna System Diversity Performance from Input Parameter Description", Electronic Letters, Vol. 39, No. 9, 1 May 2003.

[28] I. Corbella, N. Duffo, M. Vall-llossera, A. Camps and F. Torres, "The visibility function in interferometric aperture synthesis radiometry", IEEE Transactions on Geoscience and Remote Sensing, Vol. 42, Issue 8, August 2004.

[29] Hendrik Bosma, "On the Theory of Linear Noisy Systems", Doctoral Thesis, Eindhoven University, The Netherlands, 31 January 1967.

[30] M. Piera-Martinez, F. Scala, C. Colombo, A. M. Zurita, B. Duesmann, and M. Martín-Neira, "Formation Flying L-band Aperture Synthesis mission concept", In preparation for submission to TGARS

[31] M. Martín-Neira, M. Suess, J. Kainulainen, and F. Martín-Porqueras, "The Flat Target Transformation", IEEE Transactions on Geoscience and Remote Sensing, Vol. 46, No. 3, March 2008.

[32] M. Martín-Neira, R. Oliva, R. Onrubia, I. Corbella, N. Duffo, R. Rubino, J. Kainulainen, J. Closa, A. Zurita, J. del Castillo, F. Cabot, A. Khazaal, E. Anterrieu, J. Barbosa, G. Lopes, D. Barros, J. Tenerelli, R. Díez-García, V. Rodríguez, J. Fauste, J. M. Castro Cerón, A. Turiel, V. González-Gambau, R. Crapolicchio, L. Di Ciolo, G. Macelloni, M. Brogioni, F. Montomoli, P. Vogel, B. Hoyos Ortega, E. Checa Cortés, and M. Suess, "SMOS

instrument performance after more than 11 years in orbit", Proceedings of the IEEE-GRSS International Geoscience and Remote Sensing Symposium, Brussels, 12-16 July 2021.

[33] M. Martín-Neira, M. Suess, N. Karafolas, P. Piironen, F. Deborgies, B. Duesmann, E. Gandini, A. Catalán, R. Vilaseca, J. Montero, M. Puertolas, D. Outumuro, I. Corbella, N. Duffo, R. Materni, F. Piazza, S. Crivelli, T. Mengual, M. A. Piqueras, P. Villalba, J. I. Ramírez, A. Zurita, J. Closa, R. Oliva, R. Onrubia, A. Camps, J. Querol, A. Pérez-Portero, S. S. Kristensen, N. Skou, U. Liebstüecke, B. Rink, N. Jeannin, Q. García, D. Spinosa, J. M. Bjørstorp, M. Piera, F. Scala and C. Colombo, "Technology Developments towards a SMOS Follow-on Mission", ESA Living Planet Symposium, Bonn, 24-May-2022.

[34] https://www.esa.int/Enabling_Support/Space_Engineering_Technology/Shaping_the_Future/Digital_Receiver_for_Radiometer

[35] T. Mengual, P. Villalba, M. A. Piqueras, E. Rico, J.I. Ramírez, R. Vilaseca and A. Catalán, "Optical Harness and Receiver for Future L-Band Radiometer", International Conference on Space Optics 2020, France.

[36] A. Perez-Portero, J. Querol, A. Camps, M. Martin-Neira, Martin Suess, J. I. Ramirez, A. Zurita, J. Closa, R. Oliva and R. Onrubia, "RFI Detection and Mitigation for Advanced Correlators in Interferometric Radiometers", Remote Sensing 2022, 14, 4672

[37] M. Martín-Neira1 and V. Kudriashov, "Local Oscillator Concept for the Event Horizon Imager", Journal of Astronomical Instrumentation, Vol. 11, No. 3 (2022).

[38] ESA/PAT/789 - Patent application number PCT/EP2022/052898. The patent will be published in August 2023.

[39] Volodymyr V. Kudriashov, M. Martin-Neira, E. Lia, J. Michalski, P. Kant, D. Tromowicz, M. Belloni, P. Jankovic, P. Waller and M. Brandt. "Laboratory Demonstration of the Local Oscillator Concept for the Event Horizon Imager", Journal of Astronomical Instrumentation, December 2021.

[40] M.A. Brown, F. Torres, I. Corbella and A. Colliander, "SMOS Calibration", IEEE Transactions on Geoscience and Remote Sensing, Vol. 46, No. 3, March 2008.

[41] Anterrieu, E. (2007). On the reduction of the reconstruction bias in synthetic aperture imaging radiometry. IEEE Transactions on Geoscience and Remote Sensing, 45(3), 592–601.

Manuel Martín-Neira received the M.S. and Ph.D. degrees in telecommunication engineering in 1986 and 1996 respectively from the School of Telecommunication Engineering, Polytechnic University of Catalonia, Spain.

In 1988, he was awarded a fellowship to work on microwave radiometry at ESA (European Space Agency), in The Netherlands. From 1989 to 1992 he joined GMV, a Spanish firm, as responsible for several projects on GPS spacecraft precise navigation and attitude determination. Since 1992, with ESA, in charge of the radiometer activities within the Payload, Equipment and Technology Section.

He has developed new concepts for constellations of small satellites for Earth Observation. He proposed the Passive Reflectometry and Interferometry System (GNSS) to perform remote sensing with GNSS reflected signals. Since 2001 he is the Instrument Principal Engineer of ESA's Soil Moisture and Ocean Salinity (SMOS) mission, and continues to be involved in the calibration and image processing team.

Francesca Scala is a Ph.D. student at the Department of Aerospace Science and Technology at Politecnico di Milano since February 2020. Her research is focused on mission analysis, GNC and navigation for multi-satellite formation flying for interferometry application, under a mission concept founded by the European Space Agency (FFLAS) and the ERC-founded COMPASS project. Before that, she worked as Research Assistant at PoliMi, since February 2019, for the system design of the HERMES CubeSat constellation ASI mission. In 2018, she got an MEng in Space Engineering at PoliMi.

Alberto M. Zurita received the Telecommunication Engineering degree from the Universitat Politècnica de Catalunya, Barcelona, Spain, in 2007. He was with the Geoscience and Remote Sensing department of the Technische Universiteit Delft, The Netherlands, from 2006 to 2007, where he studied water content retrievals from Doppler radar measurements. In 2007 he joined the European Space Agency with a fellowship in the Mission Science Division, focusing on topography effects in L-Band radiometry. From 2008 he is with Airbus Defence and Space in Madrid, Spain, as Microwave Payload Engineer in the Microwave Instruments department. His main work focuses on early design and performance studies for future active and passive Earth Observation missions as well as supporting the SMOS in-orbit calibration and future evolutions of aperture synthesis interferometric radiometry.

Miguel Piera received the double Electrical engineering and Telecommunication Engineering degree from the Universitat Politècnica de València, Spain and Supélec, France, in 2004. Miguel obtained his PhD in applied mathematics in 2008 at the Université Paris XI, Orsay, France. Currently Miguel Piera is System Engineer at Airbus Defense and Space in Madrid since 2008. His work is focused on earth observation satellites design coordinating different spacecraft engineering disciplines from conceptual design up to implementation and in-flight tests. Before that, he worked at the European Space Agency (ESA / ESOC) with a traineeship majoring in ground stations.

Berthyl J. Duesmann, received the Geodetic Engineering master degree from the Delft Technical University, Delft, Netherlands, in 1987. After graduation he joined the Earth Observation Project department in ESTEC, the technological site of ESA in Noordwijk, Netherlands. He supported system and mission analysis for various ESA earth observation mission, from ERS-1, via ENVISAT, SMOS and GOCE to the

current Copernicus and Earth Explorer satellites. Currently Berthyl is leading the System Analysis Office, Earth Observation Directorate, ESA. The system analysis office is a small, competent team to support ESA earth observation projects in the area of system, orbit and attitude.

Matthias Drusch received the Diploma degree from Kiel University, Kiel, Germany, in 1994, and the Ph.D. and Habilitation degrees from Bonn University, Bonn, Germany, in 1998 and 2011, respectively. He was with Princeton University, Princeton, NJ, USA, and Bonn University before joining the European Centre for Medium-Range Weather Forecasts from 2002 to 2008. Since 2008, he has been with the European Space Agency as the Land Surfaces Principal Scientist at the Earth & Mission Science Division. He was the Mission Scientist for Sentinel-2 until 2014 and has been the Mission Scientist for SMOS and FLEX since 2008. His current research interests include remote sensing and radiative transfer modeling, data assimilation, hydrological modeling, and weather forecasting.

Camilla Colombo is Associate Professor at Politecnico di Milano, Italy. She currently leads the COMPASS group at the Department of Aerospace Science and Technology at Politecnico di Milano. Her research focuses on the study of natural perturbations and manoeuvres and their application to space debris modelling and mitigation, mission analysis of missions involving constellation of satellites and formation flying and mission to near-Earth asteroids. She leads several projects funded by the European Space Agency and a European Research Council Starting Grant on the project COMPASS. She serves as delegate for the Italian Space Agency at the Inter-Agency Space Debris Coordination Committee and at the COPUOS Science and Technical Subcommittee Space Mission Planning Advisory Group.

Don de Wilde received an MSc AeroSpace Engineering degree from the Technical University of Delft, The Netherlands, in 1991. He then started working at ESA/ESTEC in Noordwijk, the Netherlands, initially as a Contractor, and later as ESA Staff. He has worked from the start in the Structures section in the Mechanical Department of the Technical and Quality Management Directorate. His work focuses on ESA project support as Configuration and Structures Engineer, including Herschel, Planck, X-38, Lisa-Pathfinder, ESPRIT-HLCS, ESEO and many others. He also supports early design phase studies in the ESA Concurrent Design Facility to assess the feasibility of new and future missions. He has also supported the ESA research and development programs as Technical Officer.

Josep Closa Soteras received the degree in electronic engineering from Polythecnics University of Catalonia (UPC), Barcelona, Spain in 1997. He started his career at ESA-ESRIN working for the ENVISAT ground segment department as ASAR processor and products development engineer. He is currently the Head of the Microwave Instruments Department branch of Airbus Defence & Space in Spain. He has almost 20 years of professional activities in active and passive SAR and radiometers mission development and the associated performances, in-flight calibration activities such as the ones for ENVISAT-ASAR, PAZ (X-band SAR) and SMOS.

Erio Gandini (Senior Member, IEEE) received the M.Sc. degree in electrical engineering from the University of Modena and Reggio Emilia, Modena, Italy, in 2009, and the Ph.D. degree in electrical engineering from the University of Rennes 1, Rennes, France, in 2012. In 2011, he was a Visiting Ph.D. Student with the University of Michigan, Ann Arbor, MI, USA. In 2013, he joined the Ecole Polytechnique Fédérale de Lausanne, Lausanne, Switzerland, as a Post-Doctoral Researcher. From 2013 to 2017, he was a Post-Doctoral Researcher with the Delft University of Technology, Delft, The Netherlands. From 2016 to 2019, he was a Microwave and Antenna Scientist at the Netherlands Organization for Applied Scientific Research (TNO), The Hague, The Netherlands. In 2020, he joined the European Space Agency (ESA-ESTEC), Noordwijk, The Netherlands, where he is currently an Antenna and Submillimeter Wave Engineer.

He has authored or coauthored more than 60 scientific publications in peer-reviewed international journals and conference proceedings. He received the honorable mention at the Student Paper Competition at the International Microwave Symposium (IMS) 2012. He was a co-recipient of the Best Innovative Paper Prize at the 39th ESA Antenna Workshop in 2018.

His current research interests include array antennas, quasi-optical systems, frequency-selective surfaces, and beam-forming networks for radars, radiometers and telecommunication systems for space applications.

Roger Oliva obtained in 2004 the M.Sc degree in telecommunication engineering from the Polytechnic University of Catalonia, Spain and founded Zenithal Blue technologies in 2018, a company specialised in providing expertise assessment in Earth Observation remote sensing and in the management and detection of RFI. In his professional live, he has been working in several space projects, including the European Space Agency's mission SMOS, where he is the Calibration coordinator since 2011 and Mars Express. Roger Oliva is also leading some international initiatives in defence of the remote sensing community. He is the current chair of the IEEE GRSS

Frequency Allocation in Remote Sensing (FARS) Technical Committee, and the chair of the RFI in Remote Sensing Working Group that leads the development of a standard to quantify the amount of RFI in the remote sensing bands.

Raúl Díez-García was born in Barcelona, Spain, in 1990. He received the M.S. degree in telecommunications engineering from Universitat Politécnica de Catalunya (UPC), Barcelona, Spain, in 2014. In 2013, he was with European Space Agency (ESA-ESTEC, Noordwijk, the Netherlands). Since 2013, he has been working as Principal Earth Observation Engineer at Telespazio UK, supporting ESA's SMOS (Soil Moisture Ocean Salinity) satellite (ESA-ESAC, Madrid, Spain). Raúl is part of IDEAS-QA4EO (Instrument Data Evaluation and Analysis Service – Quality Assurance for Earth Observation), in charge of calibration and quality control support for SMOS. In addition, he is currently working towards obtaining the Ph.D. degree in Radio-Frequency Interference detection & mitigation techniques with the Passive Remote Sensing Group, Department of Signal Theory and Communications, Universitat Politécnica de Catalunya. His main research interests are in the area of microwave remote sensing and signal and image processing.

Ignasi Corbella was born in Barcelona, Spain, in 1955. He received the Telecommunication Engineering degree and Doctoral degree in telecommunication engineering from the Universitat Politècnica de Catalunya (UPC), Barcelona, Spain in 1977 and 1983, respectively.

In 1976 he was with the Microwave Laboratory, School of Telecommunication Engineering, UPC, as a Research Assistant, where he worked on passive microwave integrated-circuit design and characterization. In 1979 he was with Thomson-CSF, Paris, France, working on microwave oscillators design. In 1982 he was Assistant Professor, in 1986 Associate Professor and in 1993 Full Professor with UPC, where he is currently teaching basic microwaves and antennas at undergraduate level and graduate courses on nonlinear microwave circuits. Since 1993 he has been actively participating as a Researcher with the European Space Agency (ESA) SMOS mission in the frame of several contracts, directly with ESA, with the payload prime contractor EADS-Casa Espacio (Spain) or with operational processor prime contractor Deimos Engenharia (Portugal). His expertise includes, among others, fundamentals of interferometric aperture synthesis radiometry, radiometer calibration, image reconstruction, radiometer hardware specification and payload characterization. From 1993 to 1997 he was Academic Director of the School of Telecommunications Engineering. From 2001 to 2003 he was Director of the Department of Signal Theory and Communications, UPC. From 1998 to 1999 he was Guest Researcher at the NOAA/Environmental Technology Laboratory (Boulder-Colorado), developing methods for total-power radiometer calibration and data analysis. In 2015 he was visiting scholar in the University of Colorado at Boulder, working on emission models from layered media. From 2004 to 2010 he was been a member of the SMOS Science Advisory Group (SAG) and since 2010 of the SMOS Quality Working Group (QWG). He was the Scientific Coordinator of a Dictionary of Telecommunication terms in Catalan language, with more than 4000 entries, published in March 2007. Dr. Corbella was the General Chairman of the 2007 International Geoscience and Remote Sensing Symposium, Barcelona.